PNAS RESEARCH ARTICLE | ENGINEERING OPEN ACCESS

Harnessing elastic instabilities for enhanced mixing and reaction kinetics in porous media

Christopher A. Browne[a] and Sujit S. Datta[a,1]

Affiliations are included on p. 7.

Edited by Julio Ottino, Northwestern University, Evanston, IL; received November 28, 2023; accepted June 7, 2024

Turbulent flows have been used for millennia to mix solutes; a familiar example is stirring cream into coffee. However, many energy, environmental, and industrial processes rely on the mixing of solutes in porous media where confinement suppresses inertial turbulence. As a result, mixing is drastically hindered, requiring fluid to permeate long distances for appreciable mixing and introducing additional steps to drive mixing that can be expensive and environmentally harmful. Here, we demonstrate that this limitation can be overcome just by adding dilute amounts of flexible polymers to the fluid. Flow-driven stretching of the polymers generates an elastic instability, driving turbulent-like chaotic flow fluctuations, despite the pore-scale confinement that prohibits typical inertial turbulence. Using in situ imaging, we show that these fluctuations stretch and fold the fluid within the pores along thin layers ("lamellae") characterized by sharp solute concentration gradients, driving mixing by diffusion in the pores. This process results in a 3× reduction in the required mixing length, a 6× increase in solute transverse dispersivity, and can be harnessed to increase the rate at which chemical compounds react by 5×—enhancements that we rationalize using turbulence-inspired modeling of the underlying transport processes. Our work thereby establishes a simple, robust, versatile, and predictive way to mix solutes in porous media, with potential applications ranging from large-scale chemical production to environmental remediation.

fluid dynamics | porous media | viscoelastic | instability | mixing

Being able to efficiently mix solutes in disordered three-dimensional (3D) porous media is critical to a broad range of key energy, environmental, and industrial processes. For example, it controls the rate at which chemical compounds react in porous flow reactors (1–10) used for energy storage (11) or the production of pharmaceuticals (6–8), specialty and "green" chemicals (4, 9, 10, 12–15), biofuels (14), and functional nanomaterials (16). In these cases, the reactive solutes are transported by a fluid of density ρ and dynamic viscosity μ at a mean velocity U around solid grains of diameter d_p, such that the Reynolds number quantifying the ratio of inertial to viscous stresses $\mathrm{Re} \equiv \rho U d_p/\mu \ll 1$. Thus, the flow is expected to be laminar and steady over time, and reaction rates are limited by the slow diffusion of reactants with coefficient $\mathcal{D}$ across concentration gradients in the pores.

Moreover, the Péclet number quantifying the ratio of the reactant transport rates by advection to diffusion $\mathrm{Pe} \equiv U d_p/\mathcal{D}$ is frequently $\gg 1$. Under these conditions, "laminar chaotic advection" (LCA) (17, 18) of reactants through the tortuous pore space gives rise to appreciable mixing downstream only after traversing a large length $l_{\mathrm{mix}} \sim C d_p$, where the constant $C \gtrsim 100$ (19–24). Because this mixing length is primarily set by the fixed geometry of the medium, and cannot be appreciably shortened by changes in the imposed flow speed, it represents a fundamental limit in mixing performance. This limitation is exacerbated for chemical reactions, which proceed over a microscopic kinetic time scale τ_k after mixing, and thus require an additional reactor length $\sim \tau_k U$. Consequently, the minimum reactor length to complete the reaction increases with increasing flow speed, creating a fundamental trade-off between increasing throughput and reducing reactor length, which bears a considerable portion of capital costs (25, 26).

A similar challenge arises in many biogeochemical and environmental processes (1–3, 5, 27–37), which also rely on the mixing and dispersive spreading of reactive compounds in the subsurface. In these cases, dispersive mixing limitations necessitate the drilling of additional wells, which can be environmentally damaging and prohibitively expensive.

Here, we introduce a way to overcome these limitations by harnessing an elastic flow instability (EI) generated by polymers added to the fluid. Studies in a range of simplified

Significance

Turbulent flows are frequently used to mix solutes; a familiar example is stirring cream into coffee. However, many energy, environmental, and industrial processes rely on the flow and mixing of solutes in porous media, where confinement suppresses inertial turbulence. As a result, mixing is drastically hindered, with negative consequences for processes ranging from chemical production to environmental remediation. Here, we show that adding dilute, flexible polymers to the fluid provides a simple, robust, and versatile way to overcome this limitation. Using imaging, we demonstrate that when a polymeric fluid is injected into a porous medium, the interplay between flow and polymer stretching produces chaotic, turbulent-like flow fluctuations—greatly enhancing solute mixing and chemical reaction yield in a quantitatively predictable manner.

Author contributions: C.A.B. and S.S.D. designed research; performed research; contributed new reagents/analytic tools; analyzed data; and wrote the paper.

Competing interest statement: The method described in this publication is the subject of a patent application filed by Princeton University on behalf of the authors.

This article is a PNAS Direct Submission.

[1]To whom correspondence may be addressed. Email: ssdatta@princeton.edu.

This article contains supporting information online at https://www.pnas.org/lookup/suppl/doi:10.1073/pnas.2320962121/-/DCSupplemental.

Published July 9, 2024.

geometries have shown that the buildup of polymer elastic stresses during transport can generate chaotic flow fields reminiscent of those observed in inertial turbulence, despite the small Reynolds number (38–53). However, the opacity of more complex 3D porous media precludes visualization of the flow inside the pore space, making similar studies inaccessible. Therefore, it still remains unknown whether—and if so, how—EI can be harnessed to enhance mixing and reaction kinetics in 3D porous media. We overcome this challenge using experiments in model 3D porous media made from sintered random packings of glass beads. In particular, we formulate a dilute polymer solution whose refractive index matches that of the glass, rendering the medium transparent and enabling direct flow visualization in situ using confocal microscopy (detailed in *Materials and Methods*) (52, 54).

Results

EI Greatly Enhances Solute Mixing in a Porous Medium. To characterize solute mixing, we inject two parallel coflowing streams of fluid into the porous medium at the same imposed volumetric flow rate $Q/2$. The mean flow velocity is then $U \equiv Q/(\phi A)$, where ϕ and A are the porosity and cross-sectional area of the porous medium, respectively. As shown in Fig. 1*A*, stream A contains a nonreactive dye, which acts as a passive solute, at a concentration c_A, while stream B is undyed. We use a calibration curve to convert the dye fluorescence intensity to concentration; therefore, visualizing the fluorescence intensity at the interface between the coflowing streams provides a measure of the dye concentration c, and therefore the extent of mixing between the streams, as it varies with position x along the length of the medium. To this end, we define a dimensionless concentration $\tilde{c}(\mathbf{x}, t) = (c(\mathbf{x}, t) - c_\infty)/c_A$, where $\mathbf{x}$ is the (x, y) position vector and $c_\infty \equiv c_A/2$ is the completely mixed dye concentration, such that $\tilde{c} = 1$ and $\tilde{c} = -1$ correspond to the fully dyed and undyed streams and $\tilde{c} = 0$ represents complete mixing. Quantifying the increase in the extent of mixing with x then yields a direct measure of the mixing length l_{mix} (41, 42, 55–61). Moreover, because mixing is ultimately driven by solute diffusion across short-ranged, subpore-scale concentration gradients, we use the images to compute $\tilde{\nabla}\tilde{c} = d_p^{-1}(\partial_x + \partial_y)\tilde{c}$. Quantifying how the transverse width spanned by these concentration gradients across the medium varies with x (*SI Appendix*, Fig. S1) then yields a measure of the transverse dispersion coefficient $D_\perp^\nabla$.

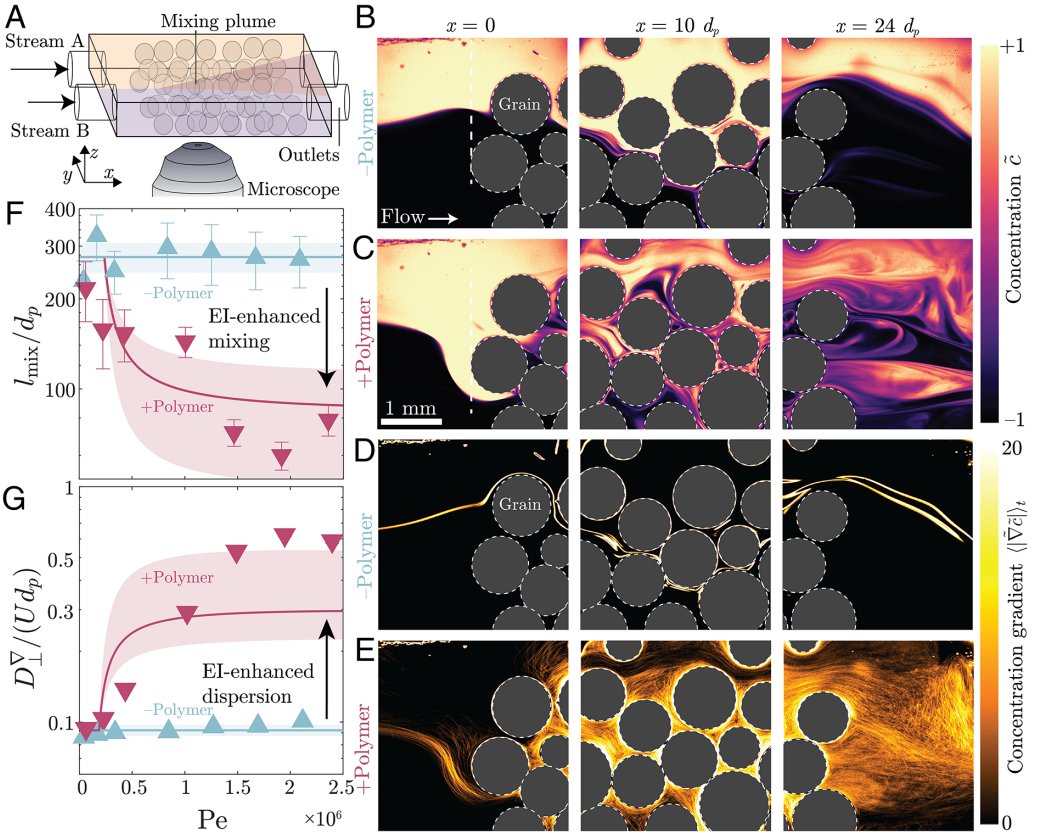

Fig. 1. In situ imaging reveals that an elastic instability greatly enhances mixing in a porous medium. (*A*) Schematic of the experiment, in which we inject two parallel coflowing streams of fluid into a model disordered 3D porous medium composed of sintered glass beads of mean diameter d_p. Stream A contains a fluorescent nonreactive dye (yellow in *B*–*E*), which acts as a passive solute, while stream B is undyed (black in *B*–*E*). We directly visualize the mixing between the streams in the 3D pore space using confocal microscopy, as shown by the optical $x-y$ slices taken at a fixed z position at the inlet ($x = 0$), middle ($x = 10\ d_p$), and outlet ($x = 24\ d_p$) of the medium in (*B*–*E*). (*B* and *C*) show the dye concentration, normalized such that $\tilde{c} = +1$ and -1 correspond to completely dyed and undyed fluid, respectively, and $\tilde{c} = 0$ therefore corresponds to completely mixed fluid, for a mean injection flow speed $U = 1.7$ mm/s. (*D* and *E*) show the corresponding normalized concentration gradient computed in the $x-y$ plane, averaged over the imaging time t. In the case of polymer-free solvent, the flow is laminar; as a result, mixing between the streams is minimal (*B*) and only occurs along a single lamellar surface, characterized by a sharp concentration gradient, along the channel centerline (*D*). Addition of polymer generates an elastic instability whose chaotic flow fluctuations dramatically improve mixing in the pore space (*C*), with lamellae of large solute concentration gradient being successively stretched and folded within the individual pores, in addition to across multiple pores (*E*). As a result, the mixing length l_{mix} decreases (*F*) and the transverse dispersion coefficient $D_\perp^\nabla$ increases (*G*) with increasing Péclet number Pe in the case of a polymeric fluid; error bars on the points represent uncertainty in determining these values from the experiments. The curves show the predictions of our theoretical model, as described further in *Materials and Methods*; the shaded region reflects the experimental uncertainty in the values of the model parameters.

In the case of polymer-free solvent, the flow remains laminar at all injection speeds tested ($\mathrm{Re} \lesssim 10^{-2}$). The two streams of fluid initially meet along a single lamellar surface along the channel centerline, characterized by a sharp concentration gradient, that is only minimally stretched and folded by LCA through the disordered pore space (Fig. 1 *B* and *D* and Movies S1 and S2). Mixing between the streams is therefore minimal. Indeed, we find a large, flow speed-independent value of $l_{\mathrm{mix}} \approx 270\ d_p$, consistent with previous studies of LCA (19–24). We also find a small, flow speed-independent value of $D_{\perp}^{\nabla} \approx 0.09\ Ud_p$, in reasonable agreement with the prediction for spherical grain packings (19, 23). These measurements are shown by the blue upward triangles in Fig. 1 *F*–*G*, respectively, which we report as a function of Pe, as is typically done.

Adding dilute polymer to the fluid dramatically changes this behavior. In this case, the flow in some pores becomes unstable, with chaotic spatiotemporal fluctuations, at a critical value of $U = U_{c,\mathrm{min}} = 170\ \mu\mathrm{m/s}$ (*SI Appendix*, Fig. S2)—reflecting the onset of EI (52). Following previous work (43–46, 50–52), we characterize this transition to unstable flow using the Weissenberg number $\mathrm{Wi} = N_1(\dot{\gamma})/(2\sigma(\dot{\gamma}))$, where the characteristic interstitial shear rate $\dot{\gamma} \equiv U/\sqrt{k/\phi}$ and k is the permeability of the medium; this dimensionless parameter compares the relative strength of flow-induced elastic stresses arising from polymer stretching, quantified by the first normal stress difference N_1, to viscous stresses, quantified by the shear stress σ. The transition to unstable flow then begins in the porous medium at $\mathrm{Wi} = \mathrm{Wi}_{c,\mathrm{min}} = 2.6$. As Wi increases above this value, more and more pores become unstable, until all the pores imaged are unstable at $\mathrm{Wi} = \mathrm{Wi}_{c,\mathrm{max}} = 4.4$, as we found previously (52).

In this case, the EI-generated flow fluctuations greatly enhance solute mixing, as shown in Fig. 1 *C* and *E* and Movies S3 and S4. Indeed, as Wi increases above $\mathrm{Wi}_{c,\mathrm{min}}$, the mixing length l_{mix} decreases below its laminar value, eventually saturating at $l_{\mathrm{mix}} \approx 80\ d_p$ for $\mathrm{Wi} > \mathrm{Wi}_{c,\mathrm{max}}$, as shown by the red downward triangles in Fig. 1*F*. The transverse dispersion coefficient $D_{\perp}^{\nabla}$ concomitantly increases to $D_{\perp}^{\nabla} \approx 0.5\ Ud_p$, as shown by the red downward triangles in Fig. 1*G*. Thus, EI gives rise to a threefold reduction in the length required to appreciably mix solutes in a porous medium, with a corresponding sixfold increase in the transverse dispersivity.

Enhanced Mixing Results from the Combination of Laminar Chaotic Advection across Many Pores and EI-Generated Chaotic Mixing in Individual Pores. Having established that EI can greatly enhance solute mixing in a porous medium, we next ask: What exact features of the unstable flow field generated by EI give rise to this enhanced mixing? And how can this link between fluid flow and solute mixing in a porous medium be described quantitatively? Close inspection of Fig. 1 *C* and *E* and Movies S3 and S4 provides a clue: EI-generated flow fluctuations appear to successively stretch and fold lamellae of large solute concentration gradient within the pores, increasing the contact area between solute and fluid, thereby promoting mixing via molecular diffusion at small scales. This process is reminiscent of the chaotic mixing generated by inertial turbulence (45, 62, 63).

To more quantitatively characterize this phenomenon, we simultaneously image the fluid velocity and solute concentration fields, $\mathbf{u}(\mathbf{x}, t)$ and $\tilde{c}(\mathbf{x}, t)$, respectively, and thereby determine the root mean square fluctuations in the magnitudes of these quantities (indicated by $'_{\mathrm{rms}}$), in individual pores. A representative example is shown in Fig. 2 *A*–*D*. As expected for EI, the flow is laminar and stable at small Wi; by contrast, at larger $\mathrm{Wi} > \mathrm{Wi}_c \approx 2.9$, we observe intermittent bursts of unstable flow (Fig. 2*A* and Movie S5) that increasingly persist with increasing Wi (teal points in Fig. 2*B*). These velocity fluctuations do not have any characteristic spatial or temporal scales. Instead, their power spectra decay as power laws, characteristic of chaotic flows (*SI Appendix*, Fig. S2) (52).

These velocity fluctuations drive fluctuations in solute concentration, which are therefore also chaotic (*SI Appendix*, Fig. S2), with their onset shifted to a larger value of $\mathrm{Wi} = \mathrm{Wi}_{c,S} \approx 4.2$ (purple points in Fig. 2*B*)—reflecting the fact that the solute stream must first enter a pore for it to become mixed by the unstable flow therein as detailed further in the *Materials and Methods*. In this case, "blobs" of solute (outlined in green in Fig. 2*C*) are progressively stretched and folded by the chaotic flow in the pore (velocity vectors shown by the arrows in Fig. 2*C*), exponentially increasing their area over time (*SI Appendix*, Fig. S3). Following previous work (64, 65), we estimate the characteristic rate of stretching by directly computing the maximal finite-time Lyapunov exponent, Γ_{EI}, from the measured fluid velocity field (66, 67). As shown in Fig. 2*E*, this characteristic stretching rate increases abruptly at the onset of EI, saturating at $\Gamma_{\mathrm{EI}} \approx 0.2\ \mathrm{s}^{-1} \approx 0.1\tau_{\mathrm{rel}}^{-1}$, where τ_{rel} is the characteristic polymer relaxation time—concomitant with the rapid decrease in l_{mix} and increase in $D_{\perp}^{\nabla}$ shown in Fig. 1. Thus, EI-generated flow fluctuations promote solute mixing within individual pores in a manner analogous to inertial turbulence, consistent with the findings of previous studies in simpler geometries (41–43, 45, 46, 61). The data indicate that Γ_{EI} may decrease slightly as Wi increases above Wi_c, perhaps due to nonlinear shear-thinning, although this is not clear given the uncertainty in the measurements; investigating this point further will be a useful direction for future study.

Motivated by these observations, we hypothesize that enhanced mixing arises from the combination of two different processes operating at different length and time scales in tandem: LCA that stretches and folds solute lamellae at a rate $\Gamma_{\mathrm{LCA}} \approx U/(270\ d_p)$ (19–24) as they are transported across multiple disordered pores (Fig. 2 *F*, *Left*), and the additional stretching and folding of lamellae within individual pores by the chaotic EI flow field at a rate $\Gamma_{\mathrm{EI}} \approx 0.1\tau_{\mathrm{rel}}^{-1}$ (Fig. 2 *F*, *Middle*), as occurs in bulk systems not exhibiting LCA but for which EI can still enhance mixing (41–43, 45, 46, 61, 68–71). The rate at which solute becomes appreciably mixed as it traverses the pore space is then given by the superposition of the two:

$$\tau_{\mathrm{mix}}^{-1} \approx \Gamma_{\mathrm{LCA}} + f\Gamma_{\mathrm{EI}}, \qquad [1]$$

where $\tau_{\mathrm{mix}}^{-1} \equiv U/l_{\mathrm{mix}}$, f represents the fraction of pores in which the solute is mixed by EI (*SI Appendix*, Fig. S2), and $\Gamma_{\mathrm{EI}} = 0$ in the purely laminar polymer-free case. The transverse dispersion coefficient can then be estimated as $D_{\perp}^{\nabla} \approx cd_p^2/\tau_{\mathrm{mix}}$, with the constant $c \approx 3$ given by our measurements in the polymer-free case. Comparing to the measurements shown in Fig. 1 *F*–*G* provides a direct test of this picture. Remarkably, we find that—despite its simplicity—Eq. **1** provides an excellent description of how EI both reduces the length required to mix solutes and increases the transverse dispersivity in a porous medium, as shown by the solid red lines in Fig. 1 *F*–*G*. This agreement between the theoretical model and our experimental measurements confirms the simple conceptual picture of EI-enhanced mixing schematized in Fig. 2*F*, thereby providing quantitative guidelines to predict and control this phenomenon in practice.

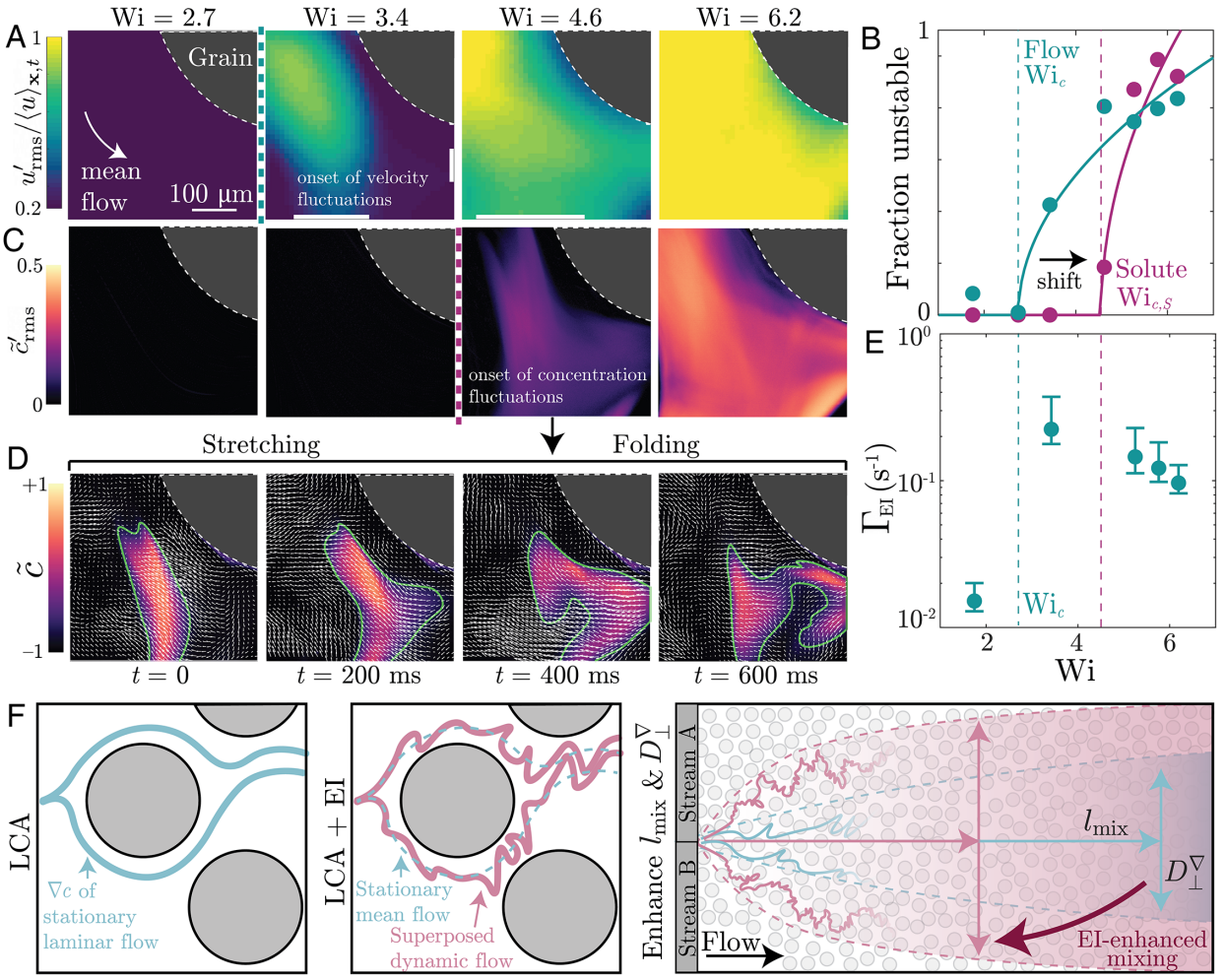

Fig. 2. EI-generated flow fluctuations stretch and fold solute lamellae in individual pores, enhancing mixing. (*A*) Magnified views of confocal $x-y$ slices taken at a fixed z position in a single pore located at $x \approx 5d_p$ and $y \approx d_p$ from the center of the medium inlet during polymer solution flow. We use fluorescent nanoparticles as tracers of the flow, enabling us to map the $x-y$ velocity field $u(\mathbf{x},t)$ via particle image velocimetry. Maps of the root mean square velocity fluctuations $u'_{\mathrm{rms}}(\mathbf{x},t)$, normalized by the mean $\langle u\rangle_{\mathbf{x},t}$, show the onset of velocity fluctuations at a critical Weissenberg number $\mathrm{Wi}_c \approx 2.9$. (*B*) The fraction of imaging time that the pore exhibits unstable velocity fluctuations for (teal points) increases continuously with Wi above $\mathrm{Wi}_c \approx 2.9$, determined from a power-law fit (teal curve). The corresponding fluctuations in normalized solvent concentration $\tilde{c}'_{\mathrm{rms}}(\mathbf{x})$ for the same pore are shown in (*C*); these fluctuations also grow continuously (magenta points in *B*). The onset of these fluctuations is shifted to a larger $\mathrm{Wi}_{c,S} \approx 4.2$, also determined from a power-law fit (magenta curve in *B*). (*D*) Snapshots at four different times for the Wi = 4.6 case, showing the normalized solute concentration $\tilde{c}$ along with the fluid velocity field shown by superposed arrows. The EI-generated chaotic flow within the pore stretches and fold the solute blob, increasing its surface area and thereby promoting mixing at the subpore scale. (*E*) Maximal finite-time Lyapunov exponent of the chaotic flow field in the pore, Γ_{EI}, abruptly increases at Wi_c, reflecting the faster stretching and folding by the fluid after the onset of EI. The data show the 90th-percentile value of the distribution of measured finite-time Lyapunov exponents, and the error bars on the points indicate the 85th and 95th percentile values. (*F*) Schematic of flow and mixing. (*Left*) In the case of polymer-free solvent, laminar chaotic advection (LCA) slightly stretches and folds solute lamellae as they transverse multiple disordered pores in the tortuous pore space (blue lines). (*Middle*) In the unstable case, EI-generated chaotic flow causes additional stretching and folding of solute lamellae within individual pores (red lines). (*Right*) The combination of LCA and EI results in a reduced mixing length and increased transverse dispersion.

EI-Enhanced Mixing Greatly Enhances Chemical Reaction Kinetics and Yield. Can this enhanced mixing be harnessed to improve the kinetics and yield of chemical reactions in porous media? To explore this possibility, we introduce a phenolic reactant, HSf, in stream A at a concentration $[\mathrm{HSf}]_0$ (magenta in Fig. 3*A*), along with an excess of sodium hydroxide in stream B (black in Fig. 3*A*). When these compounds are mixed, the HSf is irreversibly reduced to its phenolate form Sf^- (cyan in Fig. 3*A*); importantly, their peak fluorescence emission occurs at distinct wavelengths (72), enabling us to use the imaging to directly quantify reaction progress by tracking the fraction of reactant that has been converted into product, $X \equiv [\mathrm{Sf}^-]/[\mathrm{HSf}]_0$ (detailed in *Materials and Methods*).

In the polymer-free case, laminar chaotic advection only provides slight mixing between the solvent streams, and the reaction proceeds only along the midplane of the medium, shown by the *Top* row in Fig. 3*A* and Movie S6. As a result, only $\lesssim$20% of the reactant is converted to product, as shown by the blue upward triangles in Fig. 3*B*. The required porous medium length to reach a target conversion of 90%, l_{rxn}, is then $\gtrsim$100 d_p and increases with increasing Pe (blue upward triangles in Fig. 3*C*)—reflecting the typical trade-off between increasing throughput and reducing medium length in porous flow reactors. In stark contrast, the enhanced mixing generated by EI enables the reaction to proceed over a broader region of the pore space (*Bottom* row in Fig. 3*A* and Movie S7), resulting in $\gtrsim$60% conversion along the same medium length and a $\sim$5$\times$ reduction in l_{rxn} (red downward triangles in Fig. 3 *B*–*C*, respectively). Notably, l_{rxn} decreases with increasing Pe, indicating that EI-generated mixing helps overcome the trade-off between increasing throughput and reducing reactor length.

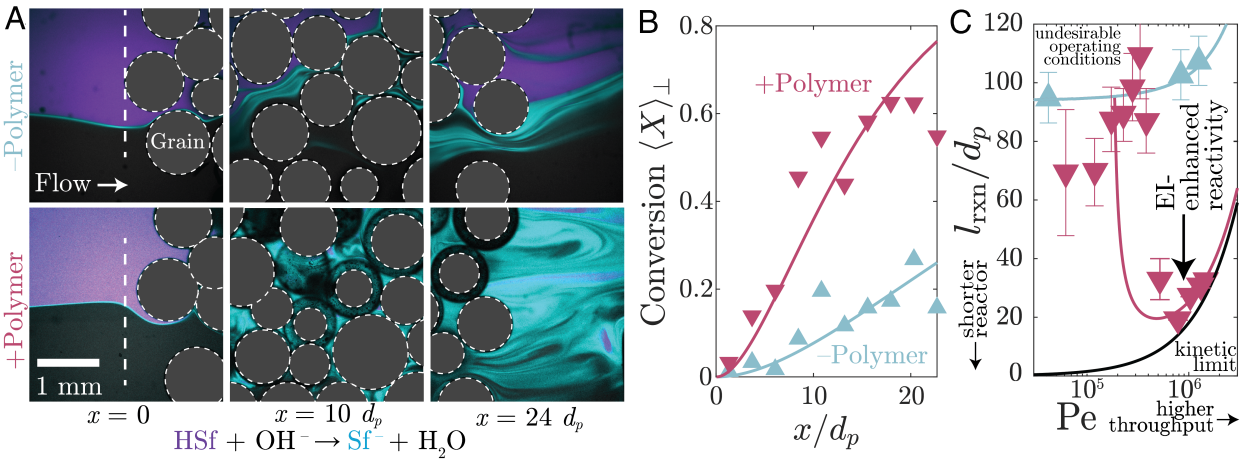

Fig. 3. EI-generated flow fluctuations enhance chemical reaction kinetics. (*A*) Confocal $x-y$ slices taken at a fixed z position at $x = 0$, 10 d_p, and 24 d_p, showing the polymer-free laminar case (*Top* row) or the unstable case of polymer solution (*Bottom* row) at $U = 1.3$ mm/s. Stream A contains the phenolic reactive dye HSf (magenta), while stream B contains the reactant OH^- along with nonreactive fluorescein dye (gray); the reaction between the two irreversibly generates the product Sf^- (cyan). (*B*) The fraction of reactant that has been converted into product X, averaged temporally and over the transverse direction y, as a function of distance x along the length of the medium. Reaction progress is minimal in the polymer-free laminar case (blue upward triangles), but approaches full conversion more rapidly in the unstable case of polymer solution (red downward triangles). Curves show Eq. **2** with $\tau_k = 11 \pm 1$ s and $\theta = 0.14 \pm 0.01$. (*C*) Extrapolating the curves in (*B*) yields the length of porous medium l_{rxn} required to reach a target conversion of $\langle X \rangle_\perp = 0.9$; in particular, we set $\langle X \rangle_\perp = 0.9$ in Eq. **2** and numerically invert to solve for l_{rxn} as a function of τ_{mix}, and then use Eq. **1** to transform this solution to one for l_{rxn} as a function of Pe instead. Error bars on the points represent uncertainty in determining these values from the fits. In the typical polymer-free laminar case, increasing throughput (increasing Pe) requires a longer reactor (blue upward triangles). EI generated by polymers breaks this trade-off between increasing throughput and decreasing reactor length (red downward triangles). Curves show theoretical predictions obtained using our lamellar mixing model (*Materials and Methods*).

Our model of enhanced mixing by successive stretching and folding of solute lamellae both across multiple pores as well as in individual pores, schematized in Fig. 2*F*, provides a way to rationalize these improvements in reaction kinetics. In particular, considering the successive mixing and reaction of solutes in differential parcels of fluid (73) yields a prediction for the macroscopic conversion (detailed in *Materials and Methods*):

$$\langle X \rangle_\perp(x) = 1 - \frac{\mathrm{Da}}{\mathrm{Da}-1}\exp\left(\frac{-x}{U\tau_k \mathrm{Da}}\right) + \frac{1}{\mathrm{Da}-1}\exp\left(\frac{-x}{U\tau_k}\right), \quad [2]$$

where the angle brackets indicate an average over the transverse direction y (denoted by the subscript $\perp$), the Damköhler number $\mathrm{Da} \equiv \theta\tau_{mix}/\tau_k$ compares the time scales of reactant mixing and reaction, where τ_{mix} is directly given by Eq. **1**, $\theta \approx 0.14$ is a constant scaling factor to account for reaction initiation before fluid is fully mixed, and $\tau_k = 11 \pm 1$ s, consistent with independent measurements (25). This prediction is in excellent agreement with the experimental measurements, as shown by the red curve in Fig. 3*B*. It also describes how EI-enhanced mixing enables *both* increased throughput and a reduced reactor length, as shown by the red curve in Fig. 3*C*. More broadly, this model indicates that EI could improve reaction kinetics even further—by as much as ~10×—when τ_k is smaller (*SI Appendix*, Fig. S5), as is the case in many other chemical reactions.

Discussion

In many energy, environmental, and industrial processes, solute mixing and chemical reaction kinetics are limited by slow diffusion during laminar flow in a porous medium. Here, we established that EI can be harnessed to overcome this limitation. This capability simply relies on the addition of dilute, flexible polymers to the fluid, and is therefore straightforward to implement in diverse settings and across a wide range of geometries. It complements other approaches that have been explored in microfluidics to overcome the diffusive limitations of typically laminar flows, which instead rely on changing the geometry of the solid boundaries surrounding the fluid (74–81) or making them flexible to enable actuation by an external controller (82–85) or promote the transition to inertial turbulence (86, 87). While tremendously useful, these approaches require making changes to the boundaries surrounding the fluid, which is often challenging or impossible to do. By contrast, our approach enhances mixing just by changing the properties of the fluid itself. In some porous media, the solid phase of the medium itself is deformable, which may help mix solutes in certain conditions (88–92); building on our work, it would be interesting to investigate whether the coupling between EI and medium deformability can result in additional enhancements in mixing.

Our in situ imaging revealed that enhanced mixing arises from the successive stretching and folding of solute lamellae by the EI-generated chaotic flow within individual pores, in addition to their stretching and folding as lamellae traverse multiple tortuous pores, in a manner reminiscent of inertial turbulence. As a result, the considerable decrease in the length of medium required to mix solute, increase in the solute transverse dispersivity, and increase in chemical reaction yield imparted by EI can all be predicted using well-established ideas from studies of turbulent flows. We anticipate that the quantitative principles we thereby developed will provide a way to predict and control EI-enhanced mixing and reaction kinetics in applications ranging from large-scale chemical production to environmental remediation (1–16, 27–37, 49). One may presume that because EI increases the pressure drop across the porous medium (52), it requires a greater amount of energy to maintain the flow and mix the fluid. However, as we show in *SI Appendix*, Fig. S7, this energy cost is offset by the dramatic reduction in the length of the medium required to mix solute—that is, not only does our approach enhance mixing and reaction kinetics, but it does so without appreciably increasing the energetic cost of pumping the fluid.

In addition to providing a capability to enhance mixing and reaction kinetics in porous media, our work also motivates further studies of the fascinating interplay between viscoelastic

fluid dynamics, solute transport and mixing, and chemical reactions. Indeed, while here we focused on a simple first-order chemical reaction as a proof of principle, our approach could be adapted to enhance the progression of other types of chemical reactions, such as reactions of other orders, reversible reactions, and solid surface-mediated reactions (93), in porous media. EI-enhanced mixing could also be used to improve heat transfer from a porous medium to an interstitial fluid, such as in heat exchangers and geothermal energy extraction. Finally, while the polymer molecules we used are chemically inert—and thus do not participate in the reaction—it would be interesting to extend our approach to the case where the polymers themselves are reactants or products, potentially driving a more complex feedback between the underlying flow and reaction rates.

Materials and Methods

Porous Media Preparation and Characterization. We prepare disordered 3D porous media following our previous work (52, 54, 94–96) by densely packing spherical borosilicate glass beads with diameters $d_p = 1{,}000$ to $1{,}400$ μm (*Sigma Aldrich*) in quartz capillaries with rectangular cross-sections of area $A = W \times H$, where the width $W = 4$ mm and height $H = 2$ mm (*Vitrocom*). Each medium is lightly sintered for ≈3 min at 1,000 °C to prevent bead rearrangements during flow, and has a length $L = 14.7 \pm 0.1$ mm and porosity $\phi \sim 0.4$. We affix two inlets and two outlets from bent 14-gauge needles (*McMaster-Carr*), whose outer diameters fit snugly into the rectangular cross-section of the capillary, glued into place with water-tight marine weld (*J-B Weld*). The inlet needles are positioned ∼1 mm away from the medium to minimize inlet and outlet effects. We determine the medium permeability $k = 624 \pm 3\ \mu m^2$ by injecting the polymer-free solvent at several flow rates $Q = 4$ to 40 mL/h, measuring the fully developed pressure drop ΔP across the medium using an *Omega PX26* differential pressure transducer and fitting to Darcy's Law $\Delta P/L = \mu Q/(kA)$.

Before each experiment, we infiltrate the porous medium with isopropyl alcohol (IPA) to prevent trapping of air and then displace the IPA by flushing with water. We then displace the water with the miscible test fluid–either the polymer solution or the polymer-free solvent. We inject our test fluids through both inlets equally at a constant total volumetric flow rate Q ranging from 0.5 to 25 mL/h using a *Harvard Apparatus* PHD 2000 syringe pump, maintaining a constant Q for each flow rate tested over 2.5 h, corresponding to over 1,000 pore volumes $t_{PV} \equiv \phi AL/Q$, before any micrographs are collected to ensure an equilibrated state. At the conclusion of the experiment, we inject rhodamine-dyed polymer-free solvent for 6 h to fully saturate the pore space with dye, and use confocal microscopy to image the pore space; the binarized images isolate the solid matrix of the porous medium, which we omit from all subsequent image analyses.

Fluid Preparation and Characterization. All of our test fluids are composed of a viscous solvent composed of 6 wt.% ultrapure *milliPore* water, 82.6 wt.% glycerol (*Sigma Aldrich*), 10.4 wt.% dimethylsulfoxide (*Sigma Aldrich*), 1 wt.% NaCl, and <0.1% additional solutes (specified further below). This formulation precisely matches the fluid refractive index to that of the glass beads $n = 1.479$, thus rendering each porous medium transparent when saturated.

We characterize the fluid rheology using steady shear measurements in an *Anton Paar* MCR301 rheometer, equipped with a 1° 5 cm-diameter conical geometry set at a 50 μm gap over a range of imposed constant shear rates $\dot{\gamma} = 0.01$ to $10\ s^{-1}$. The polymer-free solvent is Newtonian, with a constant dynamic viscosity $\mu_S = 230$ mPa · s. The polymer solution has 300 ppm of 18 MDa partially hydrolyzed polyacrylamide (*Polysciences*) added. As detailed previously (52), this solution is dilute, with an overlap concentration $c^* \approx 0.77/[\eta] = 600 \pm 300$ ppm, and the shear stress $\sigma(\dot{\gamma}_I) = A_S \dot{\gamma}^{\alpha_S}$ and first normal stress difference $N_1(\dot{\gamma}_I) = A_n \dot{\gamma}^{\alpha_n}$ with $A_S = 0.3428 \pm 0.0002$ Pa · s^{α_S}, $\alpha_S = 0.931 \pm 0.001$, $A_n = 1.16 \pm 0.03$ Pa · s^{α_n}, and $\alpha_n = 1.25 \pm 0.02$. Moreover, we describe the solution using a single polymer relaxation time $\tau_{rel} \approx \lim_{\dot{\gamma}\to 0} \frac{N_1}{2(\eta-\eta_S)\dot{\gamma}^2} = 480 \pm 30$ ms (97). This value is in good agreement with previously reported relaxation times for similar polymer and solvent compositions (40, 50, 98–100), although we expect the true longest relaxation time of the solution to be larger than this value.

Macroscopic Imaging of Solute Mixing. We use Rhodamine Red-X Succinimidyl Ester 5-isomer dye (*Invitrogen*) as a passive solute introduced into stream A at a dilute concentration $c_A = 500$ ppb; stream B is dye-free and hence $c_B = 0$. The solute diffusivity is given by $\mathcal{D} \approx 1.2 \times 10^{-8}\ cm^2/s$, obtained by extending previous measurements (101) to the case of our more viscous solvent via the Stokes–Einstein relation. We then image the solute distribution in the pore space using a *Nikon* A1R+ laser scanning confocal fluorescence microscope, continuously acquiring successive $x-y$ optical slices every 2 s at a fixed depth $z \approx 600$ μm at 10 different x positions spanning the entire length of the medium. A linear calibration curve obtained using the same imaging settings enables us to then convert fluorescence intensity to dye concentration.

To determine I_{mix}, we measure the time-averaged fraction of fluid pixels along y for which $|\tilde{c}| < 0.5$ at each position x. This fraction of well-mixed fluid increases with position as $\approx 1 - \exp(-x/l_{mix})$; fitting this relation to our data then yields the values of I_{mix} presented in Fig. 1*F*.

To determine $D_\perp^\nabla$, we use the micrographs to determine a map of the solute concentration gradient $|\nabla\tilde{c}|$, as shown in *SI Appendix*, Fig. S1. At each position x along the length of the medium, we then quantify the transverse width δ over which $|\tilde{\nabla}\tilde{c}| > \langle|\tilde{\nabla}\tilde{c}|\rangle_\perp$, where the angle brackets indicate an average over the transverse direction y (denoted by the subscript $\perp$). This plume width increases with position as $\delta(x) \approx \sqrt{\delta^2(x=0) + 2D_\perp^\nabla x/U}$; fitting this relation to our data then yields the values of $D_\perp^\nabla$ presented in Fig. 1*G*.

Many unbounded chaotic flows are characterized by an asymptotic stationary scalar probability density function (PDF) that is associated with the emergence of a dominant strange eigenmode of the advection–diffusion operator (58, 102, 103). However, we do not expect this behavior to arise in our experiments due to the particular geometry used: i) Instead of the medium being unbounded or semi-infinite, as in typical numerical studies of chaotic mixing, our experiments probe EI-induced mixing of solute in a bounded porous medium that is confined by the walls of a quartz capillary. ii) Instead of the solute being introduced as a discrete plume, it is introduced only halfway across the medium, only in one of the two coflowing streams, and mixes by spreading from the interface between the two coflowing streams in the direction transverse to the imposed flow direction. Therefore, we do not expect the scalar PDF to reach the self-similar stationary PDF that has been measured in other chaotic flows. However, exploring this possibility in other experimental geometries will be an interesting direction for future work.

Pore-Scale Imaging of Solute Mixing and Fluid Velocity Fluctuations. In addition to using Rhodamine Red-X Succinimidyl Ester 5-isomer dye as a passive solute initially in stream A, we visualize the pore-scale fluid velocity field by seeding both streams A and B with a dilute (5 ppm) suspension of $d_t = 200$ nm-diameter carboxylate-functionalized fluorescent polystyrene FluoSpheres™ (*Invitrogen*), which have a tracer Péclet number $(Q/A)d_t/\mathcal{D}_t > 10^5 \gg 1$ and thus act as passive tracers of the fluid flow; here, $\mathcal{D}_t = k_B T/3\pi\eta_0 d_t = 6 \times 10^{-3}\ \mu m^2/s$ is the tracer particle diffusivity obtained via the Stokes–Einstein relation. We monitor the flow in individual pores using a *Nikon* A1R+ laser scanning confocal fluorescence microscope, continuously acquiring successive $x-y$ optical slices of both Rhodamine and tracer particle fluorescence at 15 frames per second at a fixed depth $z \approx 600$μm. The tracer particle images are binarized and processed using particle-image velocimetry (PIV) (104) to obtain the $x-y$ fluid velocity field $\mathbf{u}(\mathbf{x}, t)$.

We estimate the characteristic rate of stretching of solute lamellae by directly computing the forward finite-time Lyapunov exponent $\Gamma_{ftle}(\mathbf{x}, t)$ from the measured velocity field for the example pore in Fig. 2; this quantity measures the exponential rate of separation of virtual tracer particles over the course of one polymer relaxation time τ_{rel}. In particular, we use an open-source code (66, 67) to numerically compute Lagrangian tracks for "virtual" tracer particles from the experimentally measured Eulerian velocity field. Each track follows pairs of

virtual tracer particles, initially seeded a differential distance apart within each pixel, integrating their trajectories forward in time, over a total duration of the polymer relaxation time, by interpolating the experimental PIV field. Virtual tracks are seeded in every imaged pixel. The separation of each virtual particle pair grows with time, and an exponential fit to this growth yields the forward-time Lyapunov exponent for that particle pair. The cumulative distribution of Γ_{ftle} thereby measured throughout the pore space is shown in *SI Appendix*, Fig. S3. We then take the 90th-percentile value as the characteristic maximal finite-time Lyapunov exponent, Γ_{EI}, which we report in Fig. 2*E*.

Interestingly, for the example pore in Fig. 2*B*, the onset of solute concentration fluctuations occurs at $\text{Wi} = \text{Wi}_{c,S} \approx 4.2$, larger than the $\text{Wi} = \text{Wi}_c \approx 2.9$ that represents the onset of fluid velocity fluctuations; further experimental corroboration of this point is given in *SI Appendix*, Fig. S2. We conjecture that this difference reflects the specific geometry of our experiments, and in practice, the values of these critical Weissenberg numbers will likely depend on the particular geometric features of how solute is introduced into the porous medium. In particular, the scalar dye is passively transported by the fluid, so if dye enters an unstable pore, we expect to immediately see concentration fluctuations. This process, however, requires dye to enter the pore in the first place–which, given the design of our experiment, depends on the location of the pore itself. At the inlet, dye is only in one of the two coflowing streams (Stream B, lower half of the porous medium). Therefore, it only enters pores in the upper half of the medium that are within the "mixing plume" generated by spreading transverse to the imposed flow direction–and indeed, it only enters a fraction of the pores therein, given the inherent pore-to-pore fluctuations in solute transport within this mixing plume as exemplified in *SI Appendix*, Fig. S1. As a result, even if a given pore is unstable ($\text{Wi} > \text{Wi}_c$), solute may not have entered it yet due to its location in the medium, and thus $\text{Wi}_{c,S} > \text{Wi}_c$. Hence, we expect that this difference between Wi_c and $\text{Wi}_{c,S}$ reflects the fact that the solute stream must first enter a pore for it to become mixed by the unstable flow therein, and we hypothesize that the exact value of $\text{Wi}_{c,S}$ will differ depending on where in the dispersion plume a given pore is. It could also be that the measurable limit of concentration fluctuations resulting from advection are nonlocal, because they require pore-to-pore communication and need a substantial number of pores to have fluctuations: This possibility is supported by the fact that the measured $\text{Wi}_{c,S} = 4.2$ is close to the upper limit shown in *SI Appendix*, Fig S2. Probing this possibility further will be a useful direction for future work.

In Situ Characterization of Chemical Reaction Kinetics. As a model chemical reaction, we choose the irreversible reduction of the fluorescent dye 5(6)-carboxy-SNARF-1 (*Fischer Scientific*) from its phenolic form HSf introduced in stream A at a concentration $[\text{HSf}]_0 = 5\ \mu\text{M}$ to phenolate form Sf^- in the presence of excess base NaOH introduced in stream B at a concentration $[\text{OH}^-]_0 = 100$ mM: $\text{HSf} + \text{OH}^- \rightarrow \text{Sf}^- + \text{H}_2\text{O}$. The reactant and product are fluorescent with distinct emission spectra (72), enabling us to map out their spatial distributions using confocal microscopy, converting fluorescence intensity to concentration using a calibration curve obtained using the same imaging settings (*SI Appendix*, Fig. S4). To visualize the pore space, stream B is additionally seeded with 1 μM of fluorescein, which does not participate in any side reactions.

Theoretical Model for Macroscopic Conversion of Reactant to Product. For a well-mixed differential parcel of fluid (denoted by the subscript WM), the reaction proceeds according to first-order reaction kinetics (25, 26, 72): $\frac{\text{d}[\text{Sf}^-]}{\text{d}t} = -k[\text{HSf}][\text{OH}^-]$, where $[\text{OH}^-] \approx [\text{OH}^-]_0$ since it is in great excess. Thus, the kinetic reaction time scale $\tau_k = \left(k[\text{OH}^-]_0\right)^{-1}$. Stoichiometric mass conservation gives $[\text{HSf}] = [\text{HSf}]_0 - [\text{Sf}^-]$, and substituting the fraction of reactant that has been converted into product in this well-mixed differential parcel of fluid, $X_{\text{WM}} \equiv [\text{Sf}^-]/[\text{HSf}]_0$, yields $X_{\text{WM}} = 1 - \exp\left(-t/\tau_k\right)$. However, this reaction can only begin to proceed in a parcel once it becomes sufficiently mixed at some time t'. The fraction of the pore space that is sufficiently mixed is then given by $f_{\text{mix}} \approx 1 - \exp\left(-t/\left(\theta\tau_{\text{mix}}\right)\right)$, where $0 < \theta \leq 1$ is a constant scaling factor to account for reaction initiation before fluid is fully mixed. Thus, integrating over all well-mixed parcels of fluid gives the macroscale conversion (73, 105): $X(t) = \int_0^t \frac{\text{d}f_{\text{mix}}}{\text{d}t}(t)\, X_{\text{WM}}\left(t - t'\right) H\left(t - t'\right) \text{d}t'$, where H is the Heaviside function, which ultimately yields Eq. **2**. To compare this prediction with our experimental measurements, we first fit the data shown in Fig. 3*B* for the three different experiments with polymer-free solvent at three different values of Pe, as shown by the blue lines in Fig. 3 *B* and *C*. These give $\tau_k = 11 \pm 1$ s and $\alpha = 0.14 \pm 0.01$ as best fits. We then apply Eq. **2**, using these same parameter values and therefore no fitting parameters, in plotting the theoretical curves for the polymer solution data in Fig. 3 *B* and *C*.

Eq. **2** appears to be singular at $\text{Da} = 1$; however, this apparent singularity is a well-known consequence of the solution to the reaction-transport equation being implicit in both Da and X. For this apparently singular value of Da, one must instead revisit the original integral equation for $X(t)$ given in the previous paragraph; simplifying this equation for $\text{Da} = 1$, integrating, and substituting $t = x/U$ then yields $X(x) = 1 - \left(1 + x/\left(U\tau_k\right)\right) e^{-x/\left(U\tau_k\right)}$, which is the alternate version of Eq. **2** suitable for the case of $\text{Da} = 1$. This equation is shown by the thin black line in *SI Appendix*, Fig. S6, which smoothly interpolates between the solutions of Eq. **2** for $\text{Da} > 1$ and $\text{Da} < 1$.

Data, Materials, and Software Availability. All study data are included in the article and/or supporting information.

ACKNOWLEDGMENTS. It is a pleasure to acknowledge stimulating discussions with Holger Stark and Reinier van Buel, laboratory support from Emily Chen, and funding support from Princeton University's Materials Research Science and Engineering Center under NSF Grant No. DMR-2011750, as well as the Camille Dreyfus Teacher-Scholar Program. C.A.B. was also supported in part by a Wallace Memorial Honorific Fellowship from the Graduate School at Princeton University.

Author affiliations: [a]Department of Chemical and Biological Engineering, Princeton University, Princeton, NJ 08544

1. J. Maree, W. F. Strydom, Biological sulphate removal in an upflow packed bed reactor. *Water Res.* **19**, 1101–1106 (1985).
2. J. Maree, W. F. Strydom, Biological sulphate removal from industrial effluent in an upflow packed bed reactor. *Water Res.* **21**, 141–146 (1987).
3. C. Tennakoon, R. Bhardwaji, J. Bockris, Electrochemical treatment of human wastes in a packed bed reactor. *J. Appl. Electrochem.* **26**, 18–29 (1996).
4. S. K. Ajmera, M. W. Losey, K. F. Jensen, M. A. Schmidt, Microfabricated packed-bed reactor for phosgene synthesis. *AIChE J.* **47**, 1639–1647 (2001).
5. S. Noorman, M. van Sint Annaland, H. Kuipers, Packed bed reactor technology for chemical-looping combustion. *Ind. Eng. Chem. Res.* **46**, 4212–4220 (2007).
6. K. Saito, M. Horie, N. Nose, K. Nakagomi, H. Nakazawa, High-performance liquid chromatography of histamine and 1-methylhistamine with on-column fluroescence derivatization. *J. Chromatogr. A* **595**, 163–168 (1992).
7. O. Trapp, Unified equation for access to rate constants of first-order reactions in dynamic and on-column reaction chromatography. *Anal. Chem.* **78**, 189–198 (2006).
8. K. Saitoh *et al.*, On-column electrochemical redox derivatization for enhancement of separation selectivity of liquid chromatography: Use of redox reaction as secondary chemical equilibrium. *J. Chromatogr. A* **1180**, 66–72 (2008).
9. F. Meirer, B. M. Weckhuysen, Spatial and temporal exploration of heterogeneous catalysts with synchrotron radiation. *Nat. Rev. Mater.* **3**, 324–340 (2018).
10. S. E. Kudaibergenov, G. I. Dzhardimalieva, Flow-through catalytic reactors based on metal nanoparticles immobilized within porous polymeric gels and surfaces/hollows of polymeric membranes. *Polymers* **12**, 572 (2020).
11. W. A. Braff, M. Z. Bazant, C. R. Buie, Membrane-less hydrogen bromine flow battery. *Nat. Commun.* **4**, 1–6 (2013).
12. S. G. Newman, K. F. Jensen, The role of flow in green chemistry and engineering. *Green Chem.* **15**, 1456–1472 (2013).
13. K. F. Jensen, Flow chemistry–microreaction technology comes of age. *AIChE J.* **63**, 858–869 (2017).
14. M. Trojanowicz, Flow chemistry in contemporary chemical sciences: A real variety of its applications. *Molecules* **25**, 1434 (2020).
15. L. Vaccaro, *Sustainable Flow Chemistry: Methods and Applications* (John Wiley & Sons, 2017).
16. S. Marre, K. F. Jensen, Synthesis of micro and nanostructures in microfluidic systems. *Chem. Soc. Rev.* **39**, 1183–1202 (2010).
17. C. Y. Lee, W. T. Wang, C. C. Liu, L. M. Fu, Passive mixers in microfluidic systems: A review. *Chem. Eng. J.* **288**, 146–160 (2016).
18. H. Song, M. R. Bringer, J. D. Tice, C. J. Gerdts, R. F. Ismagilov, Experimental test of scaling of mixing by chaotic advection in droplets moving through microfluidic channels. *Appl. Phys. Lett.* **83**, 4664–4666 (2003).

19. T. Perkins, O. Johnston, A review of diffusion and dispersion in porous media. *Soc. Pet. Eng. J.* **3**, 70–84 (1963).
20. T. Le Borgne, M. Dentz, E. Villermaux, Stretching, coalescence, and mixing in porous media. *Phys. Rev. Lett.* **110**, 204501 (2013).
21. T. Le Borgne, M. Dentz, E. Villermaux, The lamellar description of mixing in porous media. *J. Fluid Mech.* **770**, 458–498 (2015).
22. D. R. Lester, M. Dentz, T. Le Borgne, Chaotic mixing in three-dimensional porous media. *J. Fluid Mech.* **803**, 144–174 (2016).
23. M. Kree, E. Villermaux, Scalar mixtures in porous media. *Phys. Rev. Fluids* **2**, 104502 (2017).
24. J. Heyman, D. R. Lester, R. Turuban, Y. Méheust, T. Le Borgne, Stretching and folding sustain microscale chemical gradients in porous media. *Proc. Natl. Acad. Sci. U.S.A.* **117**, 13359–13365 (2020).
25. E. Guilbert, C. Almarcha, E. Villermaux, Chemical reaction for mixing studies. *Phys. Rev. Fluids* **6**, 114501 (2021).
26. E. Guilbert, E. Villermaux, Chemical reactions rectify mixtures composition. *Phys. Rev. Fluids* **6**, L112501 (2021).
27. M. M. Smith, J. A. Silva, J. Munakata-Marr, J. E. McCray, Compatibility of polymers and chemical oxidants for enhanced groundwater remediation. *Environ. Sci. Technol.* **42**, 9296–9301 (2008).
28. E. J. Anglin, L. Cheng, W. R. Freeman, M. J. Sailor, Porous silicon in drug delivery devices and materials. *Adv. Drug Deliv. Rev.* **60**, 1266–1277 (2008).
29. S. Datta *et al*., Redox trapping of arsenic during groundwater discharge in sediments from the Meghna riverbank in Bangladesh. *Proc. Natl. Acad. Sci. U.S.A.* **106**, 16930–16935 (2009).
30. P. K. Kitanidis, P. L. McCarty, *Delivery and Mixing in the Subsurface: Processes and Design Principles for in Situ Remediation* (Springer Science & Business Media, 2012), vol. 4.
31. M. L. Szulczewski, C. W. MacMinn, H. J. Herzog, R. Juanes, Lifetime of carbon capture and storage as a climate-change mitigation technology. *Proc. Natl. Acad. Sci. U.S.A.* **109**, 5185–5189 (2012).
32. K. Drescher, Y. Shen, B. L. Bassler, H. A. Stone, Biofilm streamers cause catastrophic disruption of flow with consequences for environmental and medical systems. *Proc. Natl. Acad. Sci. U.S.A.* **110**, 4345–4350 (2013).
33. J. D. Gomez-Velez, J. W. Harvey, M. B. Cardenas, B. Kiel, Denitrification in the Mississippi River network controlled by flow through river bedforms. *Nat. Geosci.* **8**, 941–945 (2015).
34. J. M. Matter *et al*., Rapid carbon mineralization for permanent disposal of anthropogenic carbon dioxide emissions. *Science* **352**, 1312–1314 (2016).
35. J. C. Stegen *et al*., Groundwater-surface water mixing shifts ecological assembly processes and stimulates organic carbon turnover. *Nat. Commun.* **7**, 1–12 (2016).
36. B. Borer, R. Tecon, D. Or, Spatial organization of bacterial populations in response to oxygen and carbon counter-gradients in pore networks. *Nat. Commun.* **9**, 1–11 (2018).
37. O. Bochet *et al*., Iron-oxidizer hotspots formed by intermittent oxic-anoxic fluid mixing in fractured rocks. *Nat. Geosci.* **13**, 149–155 (2020).
38. G. Vinogradov, V. Manin, An experimental study of elastic turbulence. *Kolloid Z. Z. Polym.* **201**, 93–98 (1965).
39. R. G. Larson, E. S. Shaqfeh, S. J. Muller, A purely elastic instability in Taylor-Couette flow. *J. Fluid Mech.* **218**, 573–600 (1990).
40. A. Groisman, V. Steinberg, Elastic turbulence in a polymer solution flow. *Nature* **405**, 53 (2000).
41. T. Burghelea, E. Segre, I. Bar-Joseph, A. Groisman, V. Steinberg, Chaotic flow and efficient mixing in a microchannel with a polymer solution. *Phys. Rev. E* **69**, 066305 (2004).
42. T. Burghelea, E. Segre, V. Steinberg, Mixing by polymers: Experimental test of decay regime of mixing. *Phys. Rev. Lett.* **92**, 164501 (2004).
43. T. Burghelea, E. Segre, V. Steinberg, Elastic turbulence in von Karman swirling flow between two disks. *Phys. Fluids* **19**, 053104 (2007).
44. C. Scholz, F. Wirner, J. R. Gomez-Solano, C. Bechinger, Enhanced dispersion by elastic turbulence in porous media. *EPL (Europhys. Lett.)* **107**, 54003 (2014).
45. M. Kumar, J. S. Guasto, A. M. Ardekani, Lagrangian stretching reveals stress topology in viscoelastic flows. *Proc. Natl. Acad. Sci. U.S.A.* **120**, e2211347120 (2023).
46. M. Kumar, D. M. Walkama, A. M. Ardekani, J. S. Guasto, Stress and stretching regulate dispersion in viscoelastic porous media flows. *Soft Matter* **19**, 6761–6770 (2023).
47. R. A. Damseh, B. Shannak, Visco-elastic fluid flow past an infinite vertical porous plate in the presence of first-order chemical reaction. *Appl. Math. Mech.* **31**, 955–962 (2010).
48. C. Sasmal, Applications of elastic instability and elastic turbulence: Review, limitations, and future directions. arXiv [Preprint] (2023). http://arxiv.org/abs/2301.02395 (Accessed 20 June 2024).
49. M. Kumar, J. S. Guasto, A. M. Ardekani, Transport of complex and active fluids in porous media. *J. Rheol.* **66**, 375–397 (2022).
50. D. M. Walkama, N. Waisbord, J. S. Guasto, Disorder suppresses chaos in viscoelastic flows. *Phys. Rev. Lett.* **124**, 164501 (2020).
51. S. J. Haward, C. C. Hopkins, A. Q. Shen, Stagnation points control chaotic fluctuations in viscoelastic porous media flow. *Proc. Natl. Acad. Sci. U.S.A.* **118**, e2111651118 (2021).
52. C. A. Browne, S. S. Datta, Elastic turbulence generates anomalous flow resistance in porous media. *Sci. Adv.* **7**, eabj2619 (2021).
53. S. S. Datta *et al*., Perspectives on viscoelastic flow instabilities and elastic turbulence. *Phys. Rev. Fluids* **7**, 080701 (2022).
54. C. A. Browne, R. B. Huang, C. W. Zheng, S. S. Datta, Homogenizing fluid transport in stratified porous media using an elastic flow instability. *J. Fluid Mech.* **963**, A30 (2023).
55. M. Chertkov, V. Lebedev, Decay of scalar turbulence revisited. *Phys. Rev. Lett.* **90**, 034501 (2003).
56. D. Son, Turbulent decay of a passive scalar in the Batchelor limit: Exact results from a quantum-mechanical approach. *Phys. Rev. E* **59**, R3811 (1999).
57. E. Balkovsky, A. Fouxon, Universal long-time properties of Lagrangian statistics in the Batchelor regime and their application to the passive scalar problem. *Phys. Rev. E* **60**, 4164 (1999).
58. G. A. Voth, T. Saint, G. Dobler, J. P. Gollub, Mixing rates and symmetry breaking in two-dimensional chaotic flow. *Phys. Fluids* **15**, 2560–2566 (2003).
59. D. Rothstein, E. Henry, J. P. Gollub, Persistent patterns in transient chaotic fluid mixing. *Nature* **401**, 770–772 (1999).
60. R. Ran *et al*., Bacteria hinder large-scale transport and enhance small-scale mixing in time-periodic flows. *Proc. Natl. Acad. Sci. U.S.A.* **118**, e2108548118 (2021).
61. A. Groisman, V. Steinberg, Efficient mixing at low Reynolds numbers using polymer additives. *Nature* **410**, 905 (2001).
62. B. I. Shraiman, E. D. Siggia, Scalar turbulence. *Nature* **405**, 639–646 (2000).
63. K. R. Sreenivasan, Turbulent mixing: A perspective. *Proc. Natl. Acad. Sci. U.S.A.* **116**, 18175–18183 (2019).
64. J. Ottino, Description of mixing with diffusion and reaction in terms of the concept of material surfaces. *J. Fluid Mech.* **114**, 83–103 (1982).
65. J. M. Ottino, *The Kinematics of Mixing: Stretching, Chaos, and Transport* (Cambridge University Press, 1989), vol. 3.
66. S. C. Shadden, J. O. Dabiri, J. E. Marsden, Lagrangian analysis of fluid transport in empirical vortex ring flows. *Phys. Fluids* **18**, 047105 (2006).
67. J. Peng, J. Dabiri, Transport of inertial particles by Lagrangian coherent structures: application to predator-prey interaction in jellyfish feeding. *J. Fluid Mech.* **623**, 75–84 (2009).
68. T. Niederkorn, J. Ottino, Mixing of a viscoelastic fluid in a time-periodic flow. *J. Fluid Mech.* **256**, 243–268 (1993).
69. S. Kumar, G. Homsy, Chaotic advection in creeping flow of viscoelastic fluids between slowly modulated eccentric cylinders. *Phys. Fluids* **8**, 1774–1787 (1996).
70. J. R. Stokes, D. V. Boger, Mixing of viscous polymer liquids. *Phys. Fluids* **12**, 1411–1416 (2000).
71. E. Afik, V. Steinberg, On the role of initial velocities in pair dispersion in a microfluidic chaotic flow. *Nat. Commun.* **8**, 468 (2017).
72. T. M. Żurawik *et al*., Revisiting mitochondrial pH with an improved algorithm for calibration of the ratiometric 5(6)-carboxy-SNARF-1 probe reveals anticooperative reaction with H^+ ions and warrants further studies of organellar pH. *PLoS One* **11**, e0161353 (2016).
73. J. Bałdyga, J. R. Bourne, *Turbulent Mixing and Chemical Reactions* (John Wiley & Sons, 1999).
74. R. H. Liu *et al*., Passive mixing in a three-dimensional serpentine microchannel. *J. Microelectromech. Syst.* **9**, 190–197 (2000).
75. A. D. Stroock *et al*., Chaotic mixer for microchannels. *Science* **295**, 647–651 (2002).
76. H. Song, M. R. Bringer, J. D. Tice, C. J. Gerdts, R. F. Ismagilov, Experimental test of scaling of mixing by chaotic advection in droplets moving through microfluidic channels. *Appl. Phys. Lett.* **83**, 4664–4666 (2003).
77. H. Song, R. F. Ismagilov, Millisecond kinetics on a microfluidic chip using nanoliters of reagents. *J. Am. Chem. Soc.* **125**, 14613–14619 (2003).
78. S. Y. Teh, R. Lin, L. H. Hung, A. P. Lee, Droplet microfluidics. *Lab Chip* **8**, 198–220 (2008).
79. X. C. i Solvas, A. DeMello, Droplet microfluidics: Recent developments and future applications. *Chem. Commun.* **47**, 1936–1942 (2011).
80. M. T. Guo, A. Rotem, J. A. Heyman, D. A. Weitz, Droplet microfluidics for high-throughput biological assays. *Lab Chip* **12**, 2146–2155 (2012).
81. L. Shang, Y. Cheng, Y. Zhao, Emerging droplet microfluidics. *Chem. Rev.* **117**, 7964–8040 (2017).
82. J. den Toonder *et al*., Artificial cilia for active micro-fluidic mixing. *Lab Chip* **8**, 533–541 (2008).
83. K. Oh, B. Smith, S. Devasia, J. J. Riley, J. H. Chung, Characterization of mixing performance for bio-mimetic silicone cilia. *Microfluid. Nanofluid.* **9**, 645–655 (2010).
84. F. Liu *et al*., An inverted micro-mixer based on a magnetically-actuated cilium made of Fe doped PDMS. *Smart Mater. Struct.* **25**, 095049 (2016).
85. B. Zhou *et al*., Design and fabrication of magnetically functionalized flexible micropillar arrays for rapid and controllable microfluidic mixing. *Lab Chip* **15**, 2125–2132 (2015).
86. M. Verma, V. Kumaran, A multifold reduction in the transition Reynolds number, and ultra-fast mixing, in a micro-channel due to a dynamical instability induced by a soft wall. *J. Fluid Mech.* **727**, 407–455 (2013).
87. V. Kumaran, P. Bandaru, Ultra-fast microfluidic mixing by soft-wall turbulence. *Chem. Eng. Sci.* **149**, 156–168 (2016).
88. M. G. Trefry, D. R. Lester, G. Metcalfe, J. Wu, Temporal fluctuations and poroelasticity can generate chaotic advection in natural groundwater systems. *Water Resour. Res.* **55**, 3347–3374 (2019).
89. G. P. Peters, D. W. Smith, Solute transport through a deforming porous medium. *Int. J. Numer. Anal. Methods Geomech.* **26**, 683–717 (2002).
90. P. J. Fox, Coupled large strain consolidation and solute transport. II: Model verification and simulation results. *J. Geotech. Geoenviron. Eng.* **133**, 16–29 (2007).
91. J. Lee, P. J. Fox, Investigation of consolidation-induced solute transport. II: Experimental and numerical results. *J. Geotech. Geoenviron. Eng.* **135**, 1239–1253 (2009).
92. M. Fiori, S. Pramanik, C. W. MacMinn, Solute transport due to periodic loading in a soft porous material. arXiv [Preprint] (2024). http://arxiv.org/abs/2402.15451 (Accessed 20 June 2024).
93. T. Aquino, T. Le Borgne, J. Heyman, Fluid-solid reaction in porous media as a chaotic restart process. *Phys. Rev. Lett.* **130**, 264001 (2023).
94. A. T. Krummel, S. S. Datta, S. Münster, D. A. Weitz, Visualizing multiphase flow and trapped fluid configurations in a model three-dimensional porous medium. *AIChE J.* **59**, 1022–1029 (2013).
95. S. S. Datta, H. Chiang, T. Ramakrishnan, D. A. Weitz, Spatial fluctuations of fluid velocities in flow through a three-dimensional porous medium. *Phys. Rev. Lett.* **111**, 064501 (2013).
96. S. S. Datta, D. A. Weitz, Drainage in a model stratified porous medium. *EPL (Europhys. Lett.)* **101**, 14002 (2013).
97. E. S. Shaqfeh, Purely elastic instabilities in viscometric flows. *Annu. Rev. Fluid Mech.* **28**, 129–185 (1996).
98. F. J. Galindo-Rosales *et al*., Microfluidic systems for the analysis of viscoelastic fluid flow phenomena in porous media. *Microfluid. Nanofluid.* **12**, 485–498 (2012).
99. A. Clarke *et al*., How viscoelastic-polymer flooding enhances displacement efficiency. *SPE J.* **21**, 675–687 (2016).
100. L. Pan, A. Morozov, C. Wagner, P. Arratia, Nonlinear elastic instability in channel flows at low Reynolds numbers. *Phys. Rev. Lett.* **110**, 174502 (2013).
101. P. O. Gendron, F. Avaltroni, K. Wilkinson, Diffusion coefficients of several rhodamine derivatives as determined by pulsed field gradient-nuclear magnetic resonance and fluorescence correlation spectroscopy. *J. Fluoresc.* **18**, 1093–1101 (2008).
102. J. Sukhatme, R. T. Pierrehumbert, Decay of passive scalars under the action of single scale smooth velocity fields in bounded two-dimensional domains: From non-self-similar probability distribution functions to self-similar eigenmodes. *Phys. Rev. E* **66**, 056302 (2002).
103. J. Heyman, D. Lester, T. Le Borgne, Scalar signatures of chaotic mixing in porous media. *Phys. Rev. Lett.* **126**, 034505 (2021).
104. W. Thielicke, E. Stamhuis, PIVlab-towards user-friendly, affordable and accurate digital particle image velocimetry in MATLAB. *J. Open Res. Softw.* **2**, e30 (2014).
105. H. Song, R. F. Ismagilov, Millisecond kinetics on a microfluidic chip using nanoliters of reagents. *J. Am. Chem. Soc.* **125**, 14613–14619 (2003).